# Supporting Information:
# Enhancing light emission with electric fields in polar nitride semiconductors

Nick Pant[1,2], Rob Armitage[3], and Emmanouil Kioupakis[2]

[1]Applied Physics Program, University of Michigan, Ann Arbor, MI, USA 48109
[2]Department of Materials Science & Engineering, University of Michigan, Ann Arbor, MI, USA 48109
[3]Lumileds LLC, San Jose, CA 95131

# Contents

.

# 1 Materials & Methods

**Poisson's equation.**
Our calculations of polarization fields are based on the Berry-phase approach to the Modern Theory of Polarization, using improper polarization constants[1] obtained with DFT employing the Heyd-Scuseria-Erznerhof (HSE) hybrid functional.[2] The Hartree-Fock mixing parameters are $\alpha = 0.31$ for GaN and AlN, and $\alpha = 0.25$ for InN, with range separation of 0.2 Å$^{-1}$, which reproduce the correct band gaps and structural properties. We calculated the strain $\epsilon$ using *ab initio* lattice and elastic constants,[3] from which we evaluated the fixed charge using Gauss's flux theorem, $\rho = -\nabla \cdot (P_{\mathrm{sp}} + e_{31}\epsilon_{11} + e_{31}\epsilon_{22} + e_{33}\epsilon_{33})$, where $P_{\mathrm{sp}}$ is the spontaneous polarization and $e_{ij}$ are piezoelectric coefficients, also calculated with the HSE functional.[1] Polarization fields are then obtained by solving Poisson's equation.

**Schrödinger's equation.**
Optical properties of materials can be accurately described by their band-edge electronic structure because carriers populate only a small fraction of the conduction-band bottom and valence-band top. We calculate properties of semiconductor heterostructures by solving the effective-mass Schrödinger equation, $\hat{H}\psi = E\psi$, where $\hat{H} = -\nabla \cdot \left[ \frac{\hbar^2}{2m^*(\mathbf{r})}\nabla \right] + V(\mathbf{r}) + q\phi(\mathbf{r})$, is represented with finite differences. Here, $m^*$ is the effective mass,[4] $\phi$ is the electrostatic potential obtained from the solution of Poisson's equation, and $V$ is the effective potential. We used band alignments obtained from accurate DFT slab calculations employing the HSE functional,[5] interpolated to intermediate compositions with composition-dependent bowing coefficients.[6, 7] We accounted for strain effects via first-principles linear deformation potentials calculated with the HSE functional.[8] We verified our results by calculating wave-function overlaps with full three-dimensional calculations, accounting for alloy disorder and summing over hundreds of eigenstates using `nextnano++`.[9] The parameters used in our calculations are provided in Tables S1-S3 of the Supporting Information.

**Variational minimization of excitons.**
We calculated the exciton binding energy by variationally minimizing the exciton Hamiltonian, $\hat{H}_{\mathrm{ex}} = \hat{H}_e + \hat{H}_h - \frac{\hbar^2}{2\mu^*}\nabla_{\boldsymbol{\rho}}^2 - \frac{\hbar^2}{2(m_e^* + m_h^*)}\nabla_{\mathbf{R}}^2 - \frac{e^2}{4\pi\epsilon}\frac{1}{\sqrt{\rho^2 + (z_e - z_h)^2}}$, where $\hat{H}_e$ and $\hat{H}_h$ are the single-particle electron and hole Hamiltonians, $\mu^*$ is the reduced effective mass, $\boldsymbol{\rho}$ is the in-plane separation vector ($\mathbf{r}_e^{\perp} - \mathbf{r}_h^{\perp}$), $\mathbf{R}$ is the center of mass coordinate, and $z_e, z_h$ are the out-of-plane coordinates of the electron and hole. Since light emission occurs from excitons with zero center-of-mass momentum, we neglected the fourth term in the exciton Hamiltonian. Excitons in a quantum well with electric fields can be calculated by making the following separable Ansatz for the wave function,[10] $\Psi_{\mathrm{ex}}^{(\lambda)}(\rho, z_e, z_h) = \psi_e(z_e)\psi_h(z_h)\phi^{(\lambda)}(\rho)$, where $\phi^{(\lambda)}(\rho) = \sqrt{\frac{2}{\pi}}\frac{e^{-\rho/\lambda}}{\lambda}$, $\lambda$ is the variational parameter and $\psi_e$ and $\psi_h$ are obtained by diagonalizing the single-particle Hamiltonians along the direction of confinement.

**Machine-learning prediction.**
We used ML surrogate models to exhaustively explore the high-dimensional configuration space of nitride quantum wells. We trained our ML models on explicit quantum-mechanical calculations of 5000 randomly sampled quantum-well configurations. We describe our ML workflow in the main text. We employed `scikit-learn`'s [11] LASSO regressor and random forests, fitting 100 decision-tree regressors on bootstrapped quantum-well configurations, allowing the nodes to expand until all leaves were pure. We tested the speedup afforded by the ML workflow using the `timeit` Python library on a laptop with 16GB random-access memory and a 2.6GHz six-core Intel Core i7 processor, with a maximum single-core frequency of 4.50 GHz. Over 70 runs, the ML prediction took 7.28 ms $\pm$ 1.63 ms per run on average, while the quantum-mechanical calculations were $339\times$ slower, taking 2.47 s $\pm$ 33.6 ms per run.

| Property | InN | GaN | AlN |
|---|---|---|---|
| $m_e^*$ $[m_0]$ | 0.07 | 0.186 | 0.33 |
| $m_h^*$ $[m_0]$ | 1.81 | 1.89 | 3.5 |
| $\varepsilon_0$ | 15 | 10 | 9 |
| $E_{\text{vbm}}^0$ [eV] | 0.61 | 0.0 | -0.46 |
| $E_{\text{cbm}}^0$ [eV] | 1.24 | 3.48 | 5.84 |
| $a_0$ [Å] | 3.548 | 3.189 | 3.112 |

Table S1: Basic material parameters [4, 5, 12, 6]

| Property | InN | GaN | AlN |
|---|---|---|---|
| $C_{13}$ | 92 | 103 | 108 |
| $C_{33}$ | 224 | 405 | 373 |

Table S2: Elastic constants [3]

| Property | InN | GaN | AlN |
|---|---|---|---|
| $a_1$ [eV] | -3.64 | -6.07 | -4.36 |
| $a_2$ [eV] | -4.58 | -8.88 | -12.35 |
| $D_3$ [eV] | 2.68 | 5.38 | 9.17 |
| $D_4$ [eV] | -1.78 | -2.69 | -3.72 |

Table S3: Deformation potentials [13]

| Property | InN | GaN | AlN |
|---|---|---|---|
| $P_{\text{sp}}$ [C/m$^2$] | 1.026 | 1.312 | 1.351 |
| $e_{31}$ [C/m$^2$] | -1.63 | 1.863 | -2.0271 |
| $e_{33}$ [C/m$^2$] | 1.238 | 1.020 | 1.569 |

Table S4: Polarization constants [1]

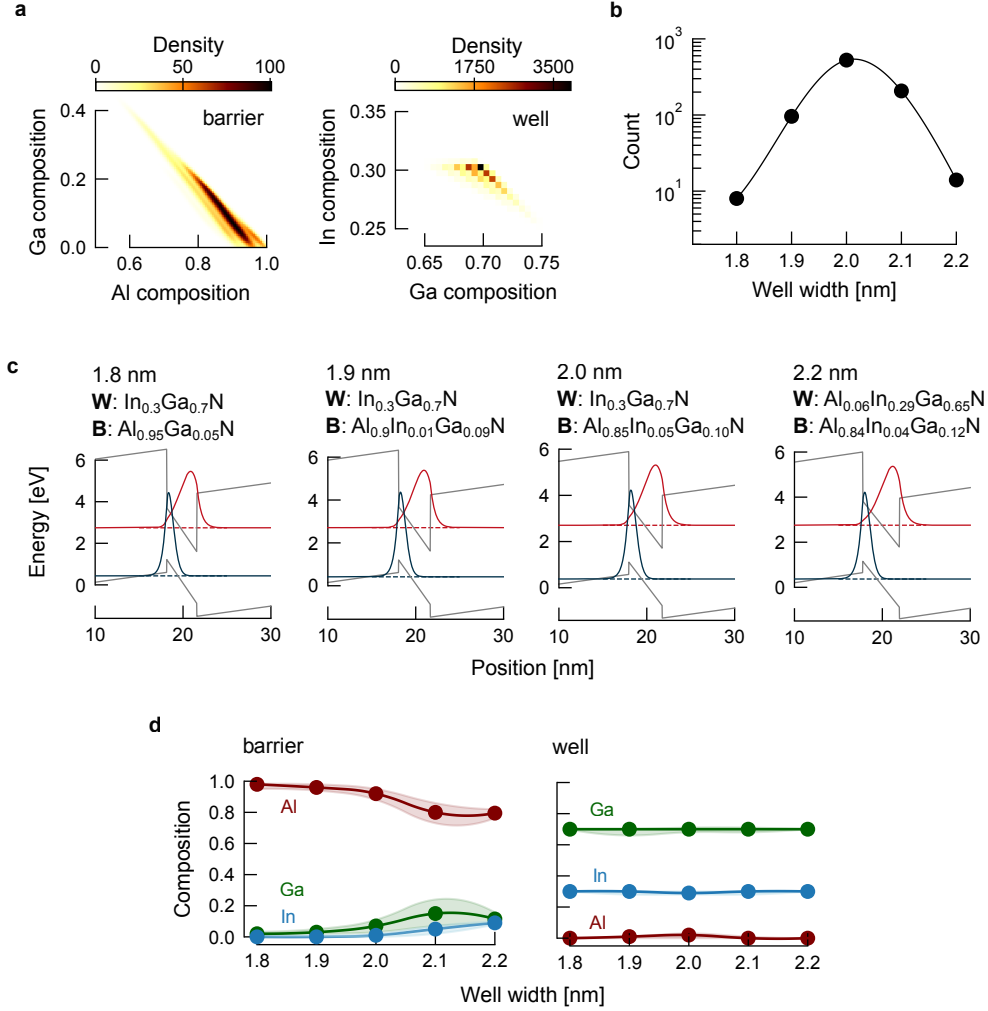# 2  Survey of the optimal red-emitting quantum wells



Figure S1: **a,** Compositional map of the optimal barriers and wells, demonstrating the region of compositional space to target during epitaxial optimization. We used Gaussian kernel-density estimation to approximate the distribution, whose density represents the number of optimal configurations per 0.005×0.005 squared units of composition. **b,** Distribution of well widths. **c,** Band diagram and electron and hole wave functions of representative configurations: W means well, B means barrier. **d,** Composition in the barriers and wells as a function of the well width: the scatter points represent the median; the shaded region correspond to the first and third quartiles. Overall, the optimal quantum wells occupy a narrow region of configuration space, with greater variation in the barrier composition than the well composition.

# 3 Calculations of wave-function overlaps with alloy disorder

To check the influence of alloy disorder on wave-function overlaps, we included alloy disorder in the Hamiltonian using `nextnano++`[9] and calculated hundreds of energy eigenstates, spanning the range from localized to extended wave functions, for four quantum-well configurations. In particular, we considered conventional 3 nm $In_{0.27}Ga_{0.73}N/GaN$ quantum wells as well as three representative optimal structures (Structure I: well $-$ 70% Ga, 30% In; barrier $-$ 72% Al, 22% Ga, 6% In. Structure II: well $-$ 4% Al, 66% Ga, 30% In; barrier $-$ 84% Al, 12% Ga, 4% In. Structure III: well $-$ 2% Al, 70% Ga, 28% In; barrier $-$ 74% Al, 26% Ga). The thermally averaged squared three-dimensional overlap of the electron and hole wave functions are an order of magnitude larger in the predicted configurations than in the reference well. Using the squared overlaps to rescale the *ab initio* bulk radiative-recombination $B$ coefficients,[14] we predict $B$ coefficients of $1.6 \times 10^{-11}$ cm$^3$/s, $9.8 \times 10^{-12}$ cm$^3$/s, and $8.2 \times 10^{-12}$ cm$^3$/s for the predicted quantum wells, in contrast to $1.7 \times 10^{-12}$ cm$^3$/s for the reference well.

# 4 Polarization fields vs improved confinement within the well

Although the Al-rich barriers confine carriers more strongly within the well because of their larger band offsets,[15, 16] it is the polarization fields that cause the primary improvement in wave-function overlap. We performed numerical control experiments to probe this hypothesis. In particular, we simulated $In_{0.3}Ga_{0.7}N/GaN$ quantum wells, artificially increasing the conduction- and valence- band offsets, in an 84:16 ratio,[5] while keeping polarization fields constant, and vice versa. For each case, we performed numerical bisection to find the well width that maintains constant emission wavelength. Although larger band offsets do improve the wave-function overlap, they also blueshift the emission. This blueshift must be compensated by increasing the well width, decreasing the overlap and negating the benefit of stronger confinement, as shown by our calculations in Fig. S2**a**. This simply means that greater confinement by barriers is not the dominant driver of overlap improvement, though it may still play a *synergistic* role. In contrast, artificially increasing the polarization field but controlling the band offset to remain constant does enhance the wave-function overlap. This is because larger fields redshift the band gap, an effect known as the quantum-confined Stark effect (QCSE), allowing the well width to decrease to maintain the same emission wavelength, as shown in S2**b**.
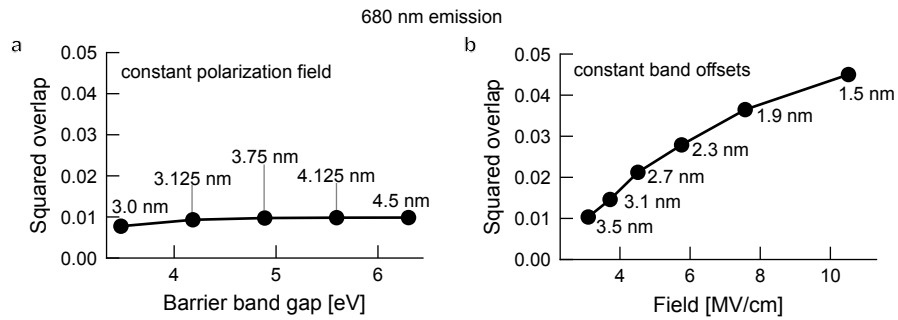


Figure S2: Numerical control experiments examining the origin of wave-function overlap improvement.**a,** Artificially increasing the band offset of the barriers while maintaining constant polarization field across the well does not improve the wave-function overlap because thicker wells are required to maintain the same red-wavelength emission, which reduces the overlap of electrons and holes. **b,** Artificially increasing the polarization field while maintaining constant band offsets between the well and the barrier does improve the wave-function overlap as it enables a reduction in well width to maintain the same red-wavelength emission. This experiment does not falsify the possibility of increased band offsets playing a secondary, synergistic role with stronger polarization fields.
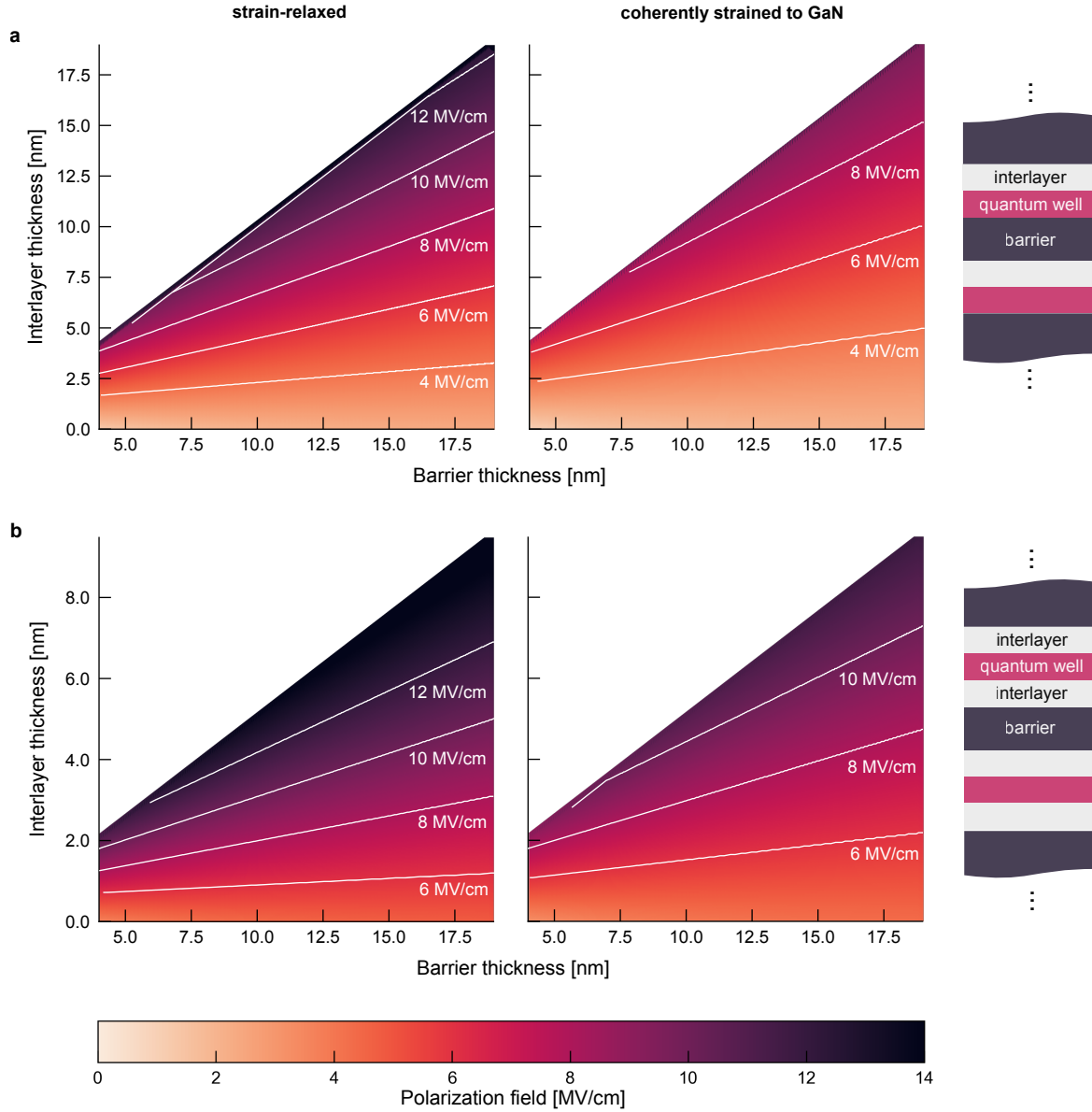
# 5 Geometric blueprint for extreme fields



Figure S3: Polarization engineering with device geometry. Map of polarization fields in periodic 2 nm wide $In_{0.3}Ga_{0.7}N$ quantum wells as a function of the GaN barrier and AlN interlayer thickness, illustrating how adjusting the heterostructure geometry enables precise control of extreme polarization fields. Designs with strain relaxation (left) enable larger fields to be realized than designs that are coherently strained to GaN (right). **a,** Interlayer on one side of the well. **b,** Interlayer on both sides of the well.
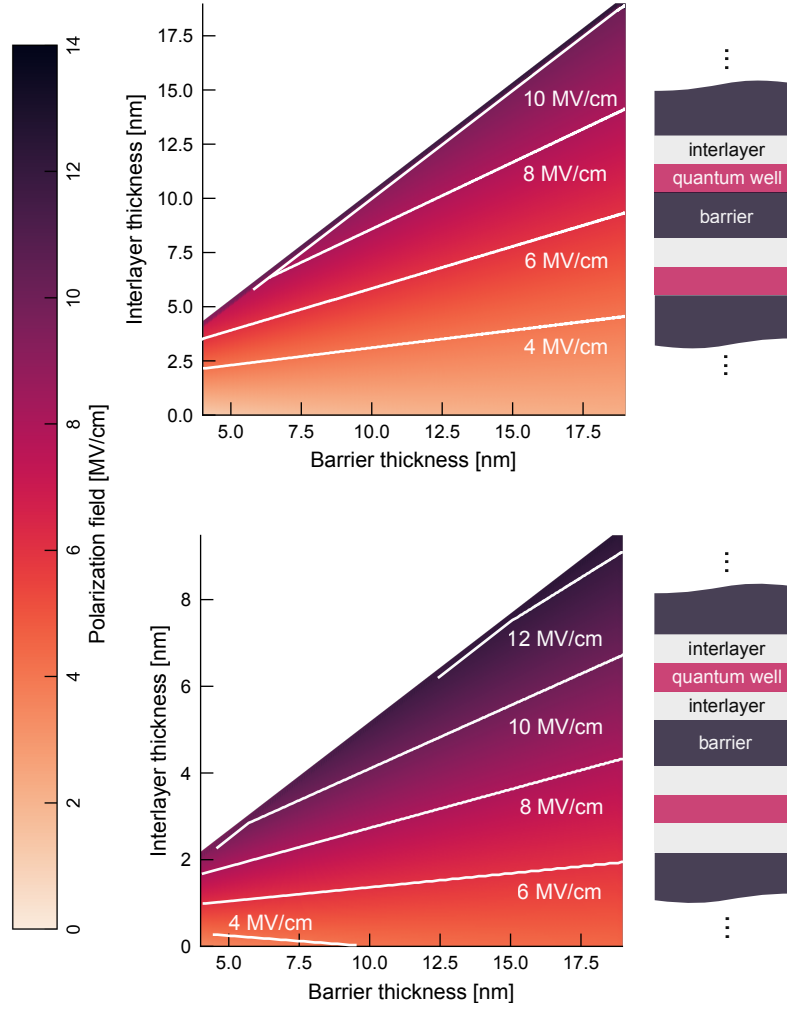
Figure S4: Polarization fields with partial strain relaxation in the quantum well. Map of polarization fields in periodic 2 nm wide $In_{0.3}Ga_{0.7}N$ quantum wells as a function of the GaN barrier and AlN interlayer thickness on $In_{0.06}Ga_{0.94}N$ substrates.

# 6 Consideration of emission broadening

Since we have modeled idealized quantum-well structure, it is important to consider how complex effects such as alloy disorder and well-width fluctuations interplay with electric fields to influence the emission.

## 6.1 Monolayer fluctuations

Emission becomes increasingly sensitive to well-width fluctuations with stronger electric fields. Although accurate emission spectra calculations require precise knowledge of these fluctuations' spatial distribution, here we present a simplified analysis that yields a first-order estimate of the characteristic energy fluctuation $\Delta E$ associated with a small well-width fluctuation $\Delta L$,

$$\Delta E = \frac{\partial \varepsilon_G^{\mathrm{QW}}}{\partial L} \Delta L \tag{1}$$

To first order, we we have neglected excitonic effects, since the binding energy of excitons is typically one to two orders of magnitude smaller than the electronic band gap $\varepsilon_G$. The band gap of the quantum well can be decomposed into contributing terms from the bulk band gap, the QCSE, and quantum confinement (in analogy with eq. 1 of the main text), $\varepsilon_G^{\mathrm{QW}} = \varepsilon_{G,\mathrm{bulk}} + \Delta\varepsilon_{\mathrm{QCSE}} + \Delta\varepsilon_{\mathrm{quantum\text{-}confinement}}$. The bulk band gap is a constant, which does not depend on the well width. The confinement of carriers in a quantum well with large electric fields occurs due to a triangular potential, which also does not depend on the well width to first order. Therefore, we can approximate the first derivative of the band gap as,

$$\frac{\partial \varepsilon_G^{\mathrm{QW}}}{\partial L} \approx \frac{\partial \Delta\varepsilon_{\mathrm{QCSE}}}{\partial L} = \frac{\partial(-eFL)}{\partial L} = -eF. \tag{2}$$

Substituting this result into eq. (1) yields the simplified expression,

$$\Delta E \approx -eF\Delta L, \tag{3}$$

where a monolayer fluctuation is $\Delta L \approx 0.3$ nm. In conventional InGaN/GaN red quantum wells, the electric field is $F \approx 4\,\mathrm{MV/cm}$, leading to a characteristic energy fluctuation of 0.12 eV or ~45 nm (assuming an emission energy of 1.86 eV). In an extreme-field quantum well where the electric field is roughly twice as large, $F \approx 8\,\mathrm{MV/cm}$, the characteristic energy fluctuation is 0.24 eV or ~85 nm. Thus, the task of achieving a narrow emission spectra becomes progressively more difficult with increasing electric fields.

## 6.2 Alloy fluctuations

The analysis above presents a lower-bound estimate for the energy fluctuation as another source of fluctuation comes from alloy disorder. Alloy fluctuations in the quantum well are important, but this does not vary as a function of the electric field since all designs that we have predicted contain roughly 30% In. In contrast, compositional fluctuations in the barrier may introduce additional broadening. The energy fluctuation of the barrier height at a composition $x$ is given by $\Delta E_{c,v} = \partial\varepsilon_{c,v}/\partial x\sqrt{x(1-x)/N}$, where $N$ is the number of cations seen by the leaked wave function within the barrier. Based on Fig. S1**c**, the wave-function leaks roughly 0.5 nm into the barrier. As a back of the envelope estimate, we approximate the lateral recombination volume with the 2D Bohr radius $R_{\mathrm{ex}} = 2\pi\epsilon\hbar^2/\mu e^2$. Using $\mu \approx 0.2$ and $\epsilon \approx 10$ gives a radius of 1.3 nm, which gives a volume of $\pi \times 1.3\mathrm{nm}^2 \times 0.5\mathrm{nm} = 2.65\,\mathrm{nm}^3$ that has leaked into the barrier; this volume contains roughly 500 cations. Due to their localized nature, excitons are more sensitive to alloy fluctuations than free carriers, therefore our estimates serve as an upper bound as we assume excitonic recombination. For the most disordered composition of AlGaN ($x = 0.5$), we use the following values, $\partial\varepsilon_c/\partial x \approx 2.0$ eV

and $\partial \varepsilon_v / \partial x \approx 1$ eV [6]. This means the effective fluctuation in the conduction band of the barrier is roughly $2$ eV $\times \sqrt{0.5 \times 0.5/500} \approx 0.04$ eV and in the valence band it is $1$ eV $\times \sqrt{0.5 \times 0.5/500} \approx 0.02$ eV. Using these values to modify the CBM and VBM in our simulations of $In_{0.3}Ga_{0.7}N/Al_{0.5}Ga_{0.5}N$ quantum wells, we found that the emission energies fluctuate by 0.01–0.02 eV; this effect is one order of magnitude weaker than due to monolayer fluctuations. We do not anticipate carrier localization to change this conclusion: if we assume that alloy disorder causes a sharper decay of the evanescent wave function into the barrier then the majority of the recombination volume will actually be within the quantum well, therefore the emission will be less sensitive to barrier compositional fluctuations. This suggests that well width fluctuations, not alloy disorder in the barrier, is the primary broadening mechanism that varies with electric fields.

# 7  Challenges associated with large electric fields

## 7.1  Competition between radiative and Auger-Meitner recombination

There are potential downsides to increasing the fields. We recently showed that the confinement of carriers by internal fields amplifies intrinsic $C$ coefficients, which quantifies non-radiative Auger-Meitner recombination.[17] This would necessitate a design trade-off between increasing the $B$ and $C$ coefficients. Increasing the $B$ coefficient would be advantageous, even at the expense of increasing the $C$ coefficient, in materials with high defect density because an increase in the light-emission probability would reduce the fraction of carriers that recombine non-radiatively over defects. Calculations by Vaxenburg et al. suggest that while electric fields enhance Auger-Meitner rates in InGaN quantum wells, the rate of increase in AMR levels off at field strengths around 4 MV/cm, which corresponds to the electric field in red-emitting InGaN/GaN quantum wells.[18] This implies that further enhancement of electric fields, as proposed in the present work, may not significantly exacerbate Auger-Meitner recombination further. However, this effect should be explicitly considered in future studies.

An additional complication is that the spectral linewidth may be sensitive to small fluctuations of the well width in the presence of strong fields, which would need to be carefully controlled. We have considered the impact of monolayer fluctuations on the emission in Section 6 of the SI.

## 7.2  Material challenges

There are also practical limits to how thick Al-containing layers can be grown on GaN before crack formation. The crack-free thickness for AlGaN on GaN templates was found experimentally to be between 50 and 100 nm for AlN mole fractions between 30% and 40%.[19] Cracking could place constraints on the total number of quantum wells and the maximum barrier thickness in LEDs with Al-rich barriers and thin InGaN wells. However, a significant part of the theoretical design space is experimentally accessible within those constraints. Moreover, we have identified designs that have minimal lattice mismatch; we present nearly-lattice-matched barrier compositions having strain of 1% or less that yield polarization fields of greater than 8 MV/cm in 2 nm $In_{0.3}Ga_{0.7}N$ quantum wells in Supplementary Dataset 2.

## 7.3  Electrical operation

We have primarily focused on the light emission from quantum wells, however further investigation is needed to integrate extreme-field designs into device architectures with high electrical-injection efficiency. One promising approach is the use of V pits, whose side walls have been shown to promote carrier injection across multiple quantum wells, particularly in the presence of Al-containing intermediate layers.[20] Another advantage of V pits is that they expose semi-polar planes with reduced electric fields, allowing for low turn-on voltages in highly polar LED structures.[21] The use of V pits in conjunction with extreme-field quantum wells confers the benefits of a semi-polar design for electrical operation while enabling enhanced light-matter coupling through extreme fields.

## 7.4  New paradigms

Quantum wells with large electric fields could be ideal candidates for alternative architectures such as blue-pump LEDs, where an electrically driven blue or violet LED optically pumps a red-emitting quantum well to achieve polychromatic emission.[22] This offers the possibility of circumventing the historical

challenges of electrical injection in conventional LED architectures through entirely novel paradigms. Finally, in Section 8 of the SI, we demonstrate that the proposed quantum wells are less prone to current overflow than conventional designs, despite their thinner wells, because the Al-containing barriers act as electron-blocking layers.

# 8  Electron overflow

Electron overflow arises when electrons are poorly confined, due to their low effective mass, and can escape thermally from the quantum well. A critical metric to consider is the energy difference between the electron subband within the well and the conduction-band minimum of the barrier. In conventional InGaN/GaN quantum wells, reducing the well thickness typically leads to increased overflow. However, the extreme-field designs with Al-containing barriers defy this trend since the barriers act as electron-blocking layers, as shown in Figure S5
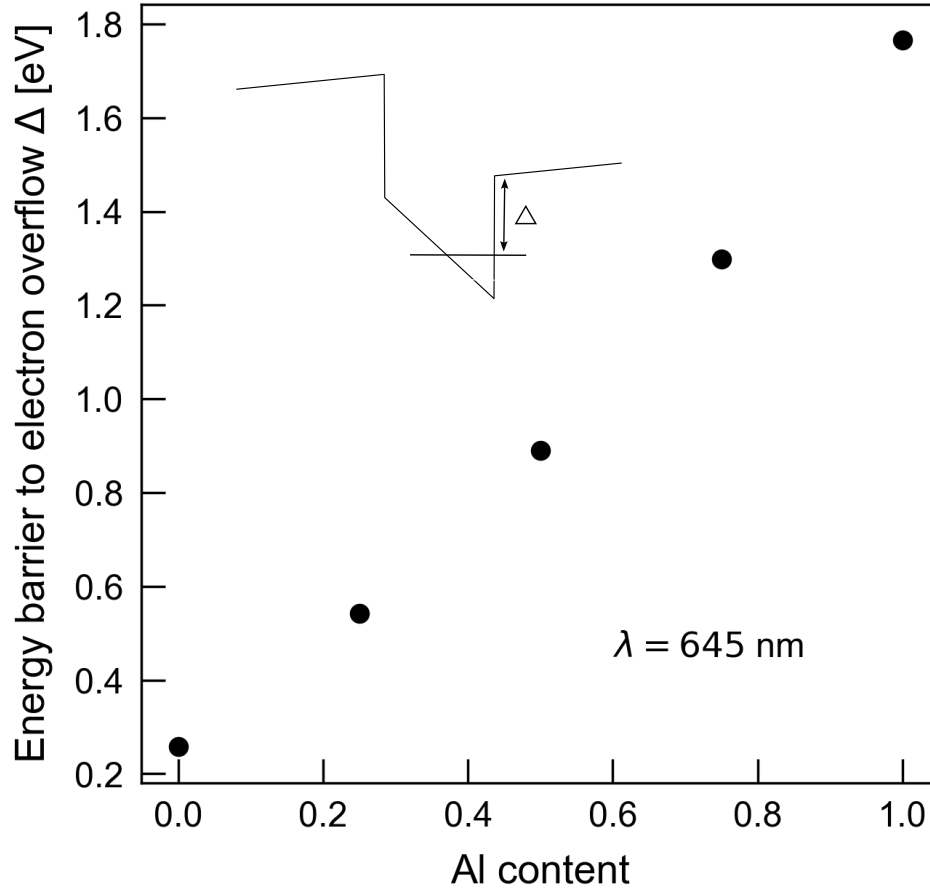


Figure S5: Energy barrier for electron overflow in $In_{0.3}Ga_{0.7}N/Al_xGa_{1-x}N$ quantum wells emitting at 645 nm. Quantum wells with higher Al content have thinner quantum wells due to higher internal electric fields. Electron overflow becomes less likely for thinner quantum well designs featuring higher Al content since the barrier acts as an electron-blocking layer.

# References

[1] Cyrus E. Dreyer et al. "Correct Implementation of Polarization Constants in Wurtzite Materials and Impact on III-Nitrides". In: *Physical Review X* 6.2 (2016-06-20), p. 021038. DOI: 10.1103/PhysRevX.6.021038. URL: https://link.aps.org/doi/10.1103/PhysRevX.6.021038 (visited on 2022-08-09).

[2] Jochen Heyd, Gustavo E Scuseria, and Matthias Ernzerhof. "Hybrid functionals based on a screened Coulomb potential". In: *The Journal of chemical physics* 118.18 (2003), pp. 8207–8215.

[3] A. F. Wright. "Elastic Properties of Zinc-Blende and Wurtzite AlN, GaN, and InN". In: *Journal of Applied Physics* 82.6 (1997-09-15), pp. 2833–2839. ISSN: 0021-8979. DOI: 10.1063/1.366114. URL: http://aip.scitation.org/doi/abs/10.1063/1.366114 (visited on 2022-08-09).

[4] Patrick Rinke et al. "Consistent Set of Band Parameters for the Group-III Nitrides AlN, GaN, and InN". In: *Physical Review B* 77.7 (2008-02-19), p. 075202. DOI: 10.1103/PhysRevB.77.075202. URL: https://link.aps.org/doi/10.1103/PhysRevB.77.075202 (visited on 2022-08-09).

[5] Poul Georg Moses et al. "Hybrid Functional Investigations of Band Gaps and Band Alignments for AlN, GaN, InN, and InGaN". In: *The Journal of Chemical Physics* 134.8 (2011-02-28), p. 084703. ISSN: 0021-9606. DOI: 10.1063/1.3548872. URL: https://aip.scitation.org/doi/full/10.1063/1.3548872 (visited on 2022-08-09).

[6] Alexandros Kyrtsos, Masahiko Matsubara, and Enrico Bellotti. "Band offsets of AlxGa1- xN alloys using first-principles calculations". In: *Journal of Physics: Condensed Matter* 32.36 (2020), p. 365504.

[7] E Iliopoulos et al. "Energy bandgap bowing of InAlN alloys studied by spectroscopic ellipsometry". In: *Applied Physics Letters* 92.19 (2008).

[8] Qimin Yan et al. "Effects of Strain on the Band Structure of Group-III Nitrides". In: *Physical Review B* 90.12 (2014-09-09), p. 125118. DOI: 10.1103/PhysRevB.90.125118. URL: https://link.aps.org/doi/10.1103/PhysRevB.90.125118 (visited on 2022-08-09).

[9] Stefan Birner et al. "nextnano: General Purpose 3-D Simulations". In: *IEEE Transactions on Electron Devices* 54.9 (2007), pp. 2137–2142. DOI: 10.1109/TED.2007.902871.

[10] P. J. Mares and S. L. Chuang. "Modeling of Self-electro-optic-effect Devices". In: *Journal of Applied Physics* 74.2 (1993-07-15), pp. 1388–1397. ISSN: 0021-8979. DOI: 10.1063/1.354897. URL: https://doi.org/10.1063/1.354897 (visited on 2023-09-24).

[11] F. Pedregosa et al. "Scikit-learn: Machine Learning in Python". In: *Journal of Machine Learning Research* 12 (2011), pp. 2825–2830.

[12] Poul Georg Moses and Chris G Van de Walle. "Band bowing and band alignment in InGaN alloys". In: *Applied Physics Letters* 96.2 (2010).

[13] Qimin Yan et al. "Band Parameters and Strain Effects in ZnO and Group-III Nitrides". In: *Semiconductor Science and Technology* 26.1 (2010-12), p. 014037. ISSN: 0268-1242. DOI: 10.1088/0268-1242/26/1/014037. URL: https://doi.org/10.1088/0268-1242/26/1/014037 (visited on 2022-08-09).

[14] Emmanouil Kioupakis et al. "Temperature and carrier-density dependence of Auger and radiative recombination in nitride optoelectronic devices". In: *New Journal of Physics* 15.12 (2013), p. 125006.

[15] Stefano Vichi et al. "Increasing the Luminescence Efficiency of Long-Wavelength (In, Ga) N Quantum Well Structures by Electric Field Engineering Using an (Al, Ga) N Capping Layer". In: *Physical Review Applied* 14.2 (2020), p. 024018.

[16] Haotian Xue et al. "Recombination Rate Analysis of InGaN-Based Red-Emitting Light-Emitting Diodes". In: *IEEE Journal of Quantum Electronics* 59.2 (2023), pp. 1–9.

[17] Nick Pant et al. "Carrier confinement and alloy disorder exacerbate Auger–Meitner recombination in AlGaN ultraviolet light-emitting diodes". In: *Applied Physics Letters* 125.2 (July 2024), p. 021109. ISSN: 0003-6951. DOI: 10.1063/5.0208840. eprint: https://pubs.aip.org/aip/apl/article-pdf/doi/10.1063/5.0208840/20041672/021109\_1\_5.0208840.pdf. URL: https://doi.org/10.1063/5.0208840.

[18]    Roman Vaxenburg et al. "The role of polarization fields in Auger-induced efficiency droop in nitride-based light-emitting diodes". In: *Applied Physics Letters* 103.22 (2013).

[19]    J-M Bethoux et al. "Growth of high quality crack-free AlGaN films on GaN templates using plastic relaxation through buried cracks". In: *Journal of applied physics* 94.10 (2003), pp. 6499–6507.

[20]    Tanay Tak et al. "Injection mechanisms in a III-nitride light-emitting diode as seen by self-emissive electron microscopy". In: *Physical Review Applied* 20.6 (2023), p. 064045.

[21]    Chi-Kang Li et al. "3D Numerical Modeling of the Carrier Transport and Radiative Efficiency for InGaN/GaN Light Emitting Diodes with V-shaped Pits". In: *AIP Advances* 6.5 (2016-05), p. 055208. DOI: `10.1063/1.4950771`. URL: `http://aip.scitation.org/doi/10.1063/1.4950771` (visited on 2022-09-02).

[22]    Benjamin Damilano and Bernard Gil. "Yellow–red emission from (Ga, In) N heterostructures". In: *Journal of Physics D: Applied Physics* 48.40 (2015), p. 403001.